Surfaces and Interfaces 38 (2023) 102773

Contents lists available at ScienceDirect

Surfaces and Interfaces

journal homepage: www.sciencedirect.com/journal/surfaces-and-interfaces

Experimental and theoretical study on the production of carbide-rich composite nano-coatings

Z. Fogarassy [a], U. Kentsch [b], P. Panjan [c], A.S. Racz [a,*]

[a] Institute for Technical Physics and Materials Science, Centre for Energy Research, Konkoly Thege M. út 29-33, H-1121 Budapest, Hungary
[b] Institute of Ion Beam Physics and Materials Research, Helmholtz-Zentrum Dresden Rossendorf, Bautzner Landstraße 400, D-01314 Dresden, Germany
[c] Jožef Stefan Institute, Jamova 39, 1000 Ljubljana, Slovenia

ARTICLE INFO

Keywords:
WC
SiC
Carbide
Irradiation
Multilayer
Mixing

ABSTRACT

Carbides are known for high hardness and corrosion resistance and therefore applicable as protective coatings. C/Si and C/W multilayers (the individual layer thicknesses were between 10 and 20 nm) have been irradiated at room temperature by argon and xenon ions. The energies varied between 40 and 120 keV while the fluences were in the range of 0.07 - 6 × 10^{16} ions/cm^2. The SRIM simulation was applied to have the proper ion energy. The irradiation induced intermixing and carbide (SiC and WC) formation at the interfaces already for the lowest irradiation fluence. The component in-depth distribution has been determined by AES depth profiling which showed that it varied greatly as a function of the irradiation conditions and layer structure. In both material pair the thickness of the produced carbide increased with square root of fluence but the mixing mechanism were different: local spike for C/W and ballistic for C/Si. The mixing efficiency was lower for the C/Si than for the C/W.

1. Introduction

Materials with superior corrosion resistance, mechanical durability and high heat resistance are essentially important in harsh environment applications. Among others carbides are often used as protective coatings. The production of carbides needs high temperature and high pressure processes, in which many substrates cannot with stand such conditions. However, stable material can be produced by far from equilibrium conditions method. It is possible to produce compounds and metastable phases at room temperature by applying ion irradiation [1]. It can be also used to form surface nano-patterns [2,3]. If we irradiate a layer structure at the interfaces atomic mixing, or ion beam mixing (IBM) happens and compound formation might occur as well. Gupta et al. synthesized PbTe nanocrystals using low energy ion beam mixing (90 keV $Ar^+$and 140 keV Kr^+ions) of a Te/Pb bilayer on a Si substrate [4]. Arranz et al. investigated the mixing of Ti and Al layers by 2–3 keV nitrogen ions [5]. Galindo et al. produced chromium-silicon mixed oxides by mixing of Cr/Si bilayer by 80 keV oxygen ions [6]. Thabethe et al. observed the formation of WSi_2 and WC phases in the case of irradiating a W-SiC sample by Xe^{26+}in the high energy regime (MeV) [7]. Bilayers are irradiated in most of the cases which strongly limits the thickness of the produced layer. The application of multilayers helps in tuning the thickness of the produced layer and the amount of compound present at each interfaces. Multilayers have also importance in the design of radiation-resistant materials for nuclear purposes. It has been shown that nanoscale metallic multilayers (NMMs) display higher hardness than their bulk crystals counterparts, also characterized by their high radiation-induced damage tolerance which is achieved by enhancing defect recovery via interfaces [8,9]. However, the potential use of low energy IBM on multilayer structures to produce compounds which are base of protective coatings is less explored.

Silicon carbide (SiC) became a key material in the semiconductor industry. It is being increasingly used to replace Si in the fabrication of micro-electromechanical systems (MEMS) devices due to its high heat resistance, high hardness and extremely inertness to chemicals [10]. Due to these properties it is also used as protective coating. It was applied to stabilize Si-based anodes by inhibiting chemical reactions [11]. It was applied as protective layer in photovoltaic retinal prostheses [12]. SiC is also known as a radiation resistive material therefore it is a structural material candidate in the next generation fission reactors [13]. Tungsten carbides (WC) have also a wide range of existing and potential applications. The superior hardness, low friction co-efficient, and thermal stability of tungsten carbides are a few of the properties leading to its tribological application as a wear and corrosion-resistant

* Corresponding Author.
E-mail address: racz.adel@ek-cer.hu (A.S. Racz).

https://doi.org/10.1016/j.surfin.2023.102773
Received 26 October 2022; Received in revised form 7 February 2023; Accepted 24 February 2023
Available online 4 March 2023

Table 1
Summary of the projected ranges (nm) with longitudinal straggling for different C/Si and C/W layer structures, projectiles and energies.

	40 keV Xe^+	120 keV Xe^+	40 keV Ar^+	110 keV Ar^+
102010-W	14 ± 3	25 ± 10	20 ± 11	–
2020-W	–	–	29 ± 10	52 ± 25
1020-Si	–	57 ± 12	42 ± 15	–
2020-Si	–	54 ± 11	40 ± 13	–

coating [14–16]. It has been also applied as a thin-film diffusion barrier and a Schottky contact in high temperature electronics [17]. In recent years it is gaining more importance as an electrocatalyst, as well [18–20].

During the irradiation of bilayers and multilayers structures, ions locally deposit large amounts of energy and induce strong atomic rearrangement interface mixing and chemical reactions might take place. Ion beam mixing is influenced by various parameters such as deposited energy density, ion fluence, atomic mass, atomic number of the target material and incident ions. There are several models available for explaining the ion beam mixing mechanism. It has been suggested that, for energies in the range of few keV per nucleon and targets with an average atomic number $Z_{av}<20$, the elastic collisions with the target atoms are the dominant energy loss mechanism of ions (nuclear energy loss regime), the mixing is governed by ballistic transport processes [21]. For higher average atomic numbers generally higher mixing rates have been observed. The thermal spike model was created for explaining this observation which considers a spike as “a limited volume inside a solid with the majority of atoms temporarily in motion”. Here the thermochemical driving forces (heat of mixing and cohesive energy) play an important role. The thermal spike can be local or global, which depends on the damage energy density deposited at the interface [22]. These models exist at low ambient temperature while at "high" ambient temperatures, radiation-enhanced diffusion can play a dominant role [23].

Previously we have shown that SiC and WC-rich layers can be produced by irradiating C/metal multilayer structures; the produced layers exhibited excellent corrosion resistive properties [24–26]. The detailed study and the comparison of the layer production and the investigation of the possible mixing mechanisms are missing. The main aim of this work is to assess the potential use of IBM to produce carbide rich films and to investigate the different mixing mechanisms. We present the results of noble gas (energy range 40–120 keV) ions induced ion beam mixing of C/W and C/Si multilayer structures. It will be shown that WC and SiC layers of desired thickness will be produced in this way by changing the ion energy, fluence and initial layer thicknesses. The initial structure and the irradiated samples were studied by transmission electron microscopy while the distribution of the elements was analyzed by Auger Electron Spectroscopy (AES) depth profiling. A detailed recipe will be given for producing the carbide-rich layers applicable as protective coatings. We provide a comparative study on the possible mixing mechanism.

2. Experimental section

2.1. Production of SiC and WC-rich layers

Several C/Si and C/W multilayer structures were produced by sputter deposition of W, Si, and C. In both cases Si single crystal was the substrate. The samples differed in the number and the thickness of the layers. The sputtering was performed in a Balzers Sputron sputtering chamber. A plasma beam (typically 40 V/40 A) is produced between the hot filament and the auxiliary anode around the target. The pyrolitic graphite and the silicon/tungsten (99.99%) targets with a diameter of 60 mm are interchangeable in situ. The sputtering voltage was held constant at 1700 V with 0.6 A of target current. The substrates were positioned far from the plasma therefore it was possible to keep the substrate temperature during deposition process below 100 °C. The thickness of the sputtered layer was controlled by quartz-crystal microbalance.

The initial structure of the specimens was determined by cross-sectional transmission electron microscope (XTEM). The XTEM measurements were performed in a FEI-Themis Cs-corrected (scanning) transmission electron microscope, in both HREM (High Resolution Electron Microscope) and STEM (Scanning Transmission Electron Microscope) mode (point resolution is around 0.09 nm in HRTEM mode and 0.16 nm in STEM mode) operated at 200 kV. The sample preparation for XTEM was made by FIB ion milling. The actual thicknesses for the different layer systems were found to be C 10.4 nm / W 24.5 nm / C 9.2 nm // Si substrate; C 15.8 nm / W 22.7 nm / C 17.2 nm / W 24.3 nm / C 21.1 nm // Si substrate; C 20 nm / Si 20 nm / C 19 nm / Si 23 nm / C 17.5 nm // Si substrate and C 11 nm / Si 22 nm / C 11 nm / Si 22 nm / C 11 nm // Si substrate. For easier reference we call these samples as 102010-W; 2020-W; 1020-Si; 2020-Si, respectively.

The WC-rich layer was produced by irradiating the multilayer structures by Ar^+ or Xe^+ions at room temperature. The irradiation was performed at Helmholtz Zentrum Rossendorf Dresden in a High Voltage Engineering Europa B.V., Model B8385 implanter. The samples were fixed to the sample holder with a carbon tape. The applied energy for argon was 40–110 keV, the fluences were 0.1 - 6 × 10^{16} Ar^+/cm^2. In the case of xenon, the energy varied between 40 and 160 keV, while the fluences were 0.07 - 3 × 10^{16} Xe^+/cm^2. The SiC-rich layers have been produced in the Wigner Heavy ion cascade implanters. The applied energy for argon was 40 keV, the fluences were 0.5 - 6 × 10^{16} Ar^+/cm^2; while for xenon 120 keV ion energy and 0.25 - 3 × 10^{16} Xe^+/cm^2 fluences have been applied.

For having a fair understanding of the mixing we have performed many experiments varying the layer structures, projectiles, energies, and fluences. Based on the Monte-Carlo simulation using the SRIM code [27], the energy of the ions in most cases was chosen in such a way that the irradiating ions reach all interfaces. The calculated ion ranges are summarized in Table 1 for all layer structures and irradiations.

Fig. 1 depicts simulation examples for the C/W and C/Si layer structures for different argon energies. Fig. 1a and b shows the penetration depths calculated by the SRIM [31] simulation for C/W 2020 layer structure for argon ion energies 40 and 110 keV, respectively. It can be seen that the ion ranges are strongly different. In the case of irradiation 40 keV the last carbon layer is not reached by the ions. At the same time in the case of 110 keV irradiation due to the higher projected range the ions penetrate deeper into the sample, the last carbon layer and also the Si substrate is reached. It is interesting to plot the results of SRIM simulation again for 40 keV argon energy (Fig. 3c) but for the C/Si 2020 system. In the case of the “lighter” target the same applied energy penetrates deeper to the sample than in the case of the C/W sample.

2.2. AES depth profiling

After ion irradiation the samples were measured by AES depth profiling to obtain the composition of the samples along the depth. The Auger spectra were recorded by a STAIB DESA 150 pre-retarded Cylindrical Mirror Analyzer (CMA) in direct current mode. For the depth profiling 1 keV Ar^+ ions were used. The ion current was kept constant during sputtering. The samples were rotated (6 rev/min) during ion bombardment. For the case of C/Si system the angle of incidence for Ar^+ ions was 80° with respect to the surface normal. These parameters are our generally applied conditions which are chosen for minimizing the ion bombardment-induced surface and interface morphology changes [32]. However, for the C/W system, due to the large difference between the sputtering yields of C and W, 60° angle of incidence has been applied.

The shapes and energies of the C (KLL) Auger peak in carbide and graphite phases are different, thus based on these differences the

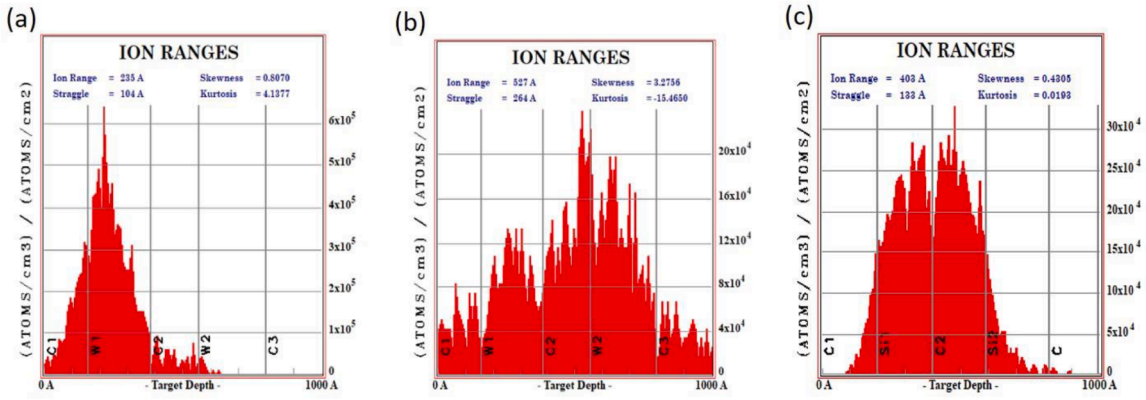

Fig. 1. Ion ranges simulated by SRIM for samples a. 2020-W Ar^+ ion 40 keV b. 2020-W Ar^+ ion 110 keV c. 2020-Si Ar^+ ion 40 keV.

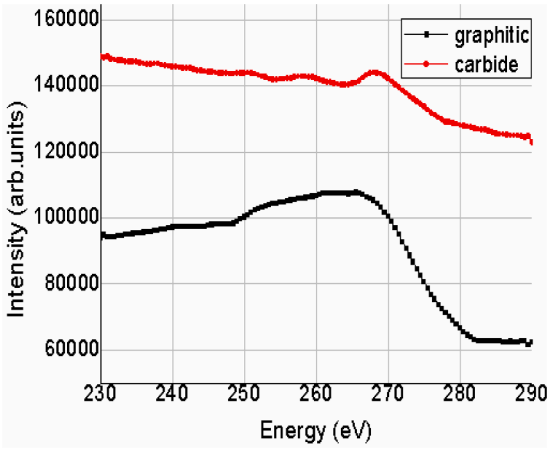

Fig. 2. Auger non-differentiated spectra for the graphitic and carbide components.

measured C Auger peak could be decomposed into graphitic and carbide components, as shown in Fig. 2. The experimentally measured Auger peak decomposition has been performed by applying the CasaXPS program [33]. Hence the AES analysis provided the depth distributions of C, W, WC, Si and the bombarding projectile. The relative sensitivity factor method [34] was used for the calculation of the atomic concentrations. The sputtering time was transformed to the removed thickness by applying our previously elaborated method [35].

3. Results and discussion

3.1. XTEM results

XTEM imaging was used to characterize the initial and final (irradiated) structures of the samples. EDS helps to identify the different regions in the sample. Fig. 3a shows the HAADF (high-angle annular dark field) XTEM image of the 102010-W pristine sample. We can see layers of different thicknesses deposited on a crystalline substrate. The contrast is influenced by the atomic number, so that the darker regions belong to carbon, while the brighter region corresponds to W which has higher atomic number. The thickness of the two carbon layers is approximately the same, the tungsten layer is placed between these two layers, all interfaces are sharp. Fig. 3b shows the corresponding EDS map which strengthens these findings. Additionally, we can see the platinum protective layer from the FIB lamella preparation.

Fig. 4a shows the XTEM image in HAADF mode of the pristine C/Si

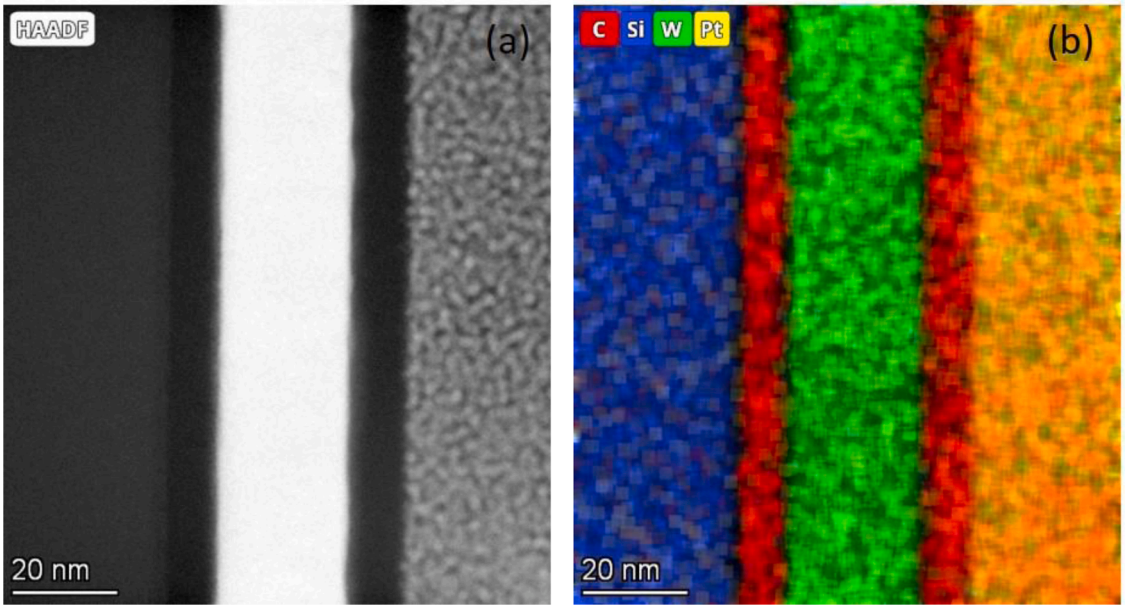

Fig. 3. a. HAADF XTEM image with the corresponding b. EDS map of the C/W specimen 102010-W pristine sample.

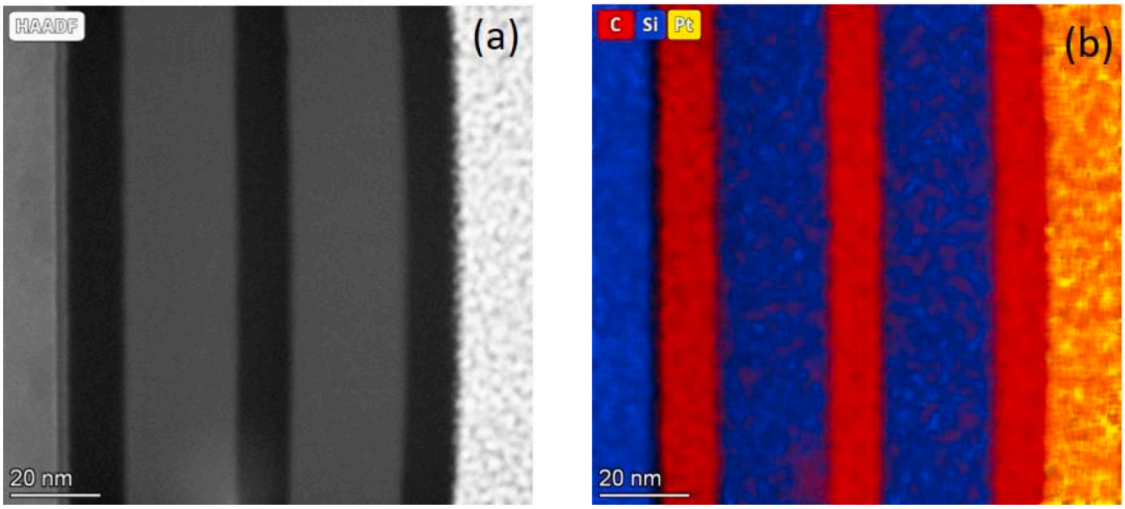

Fig. 4. a. HAADF XTEM image with the corresponding b. EDS map of the C/Si specimen 1020-Si pristine sample.

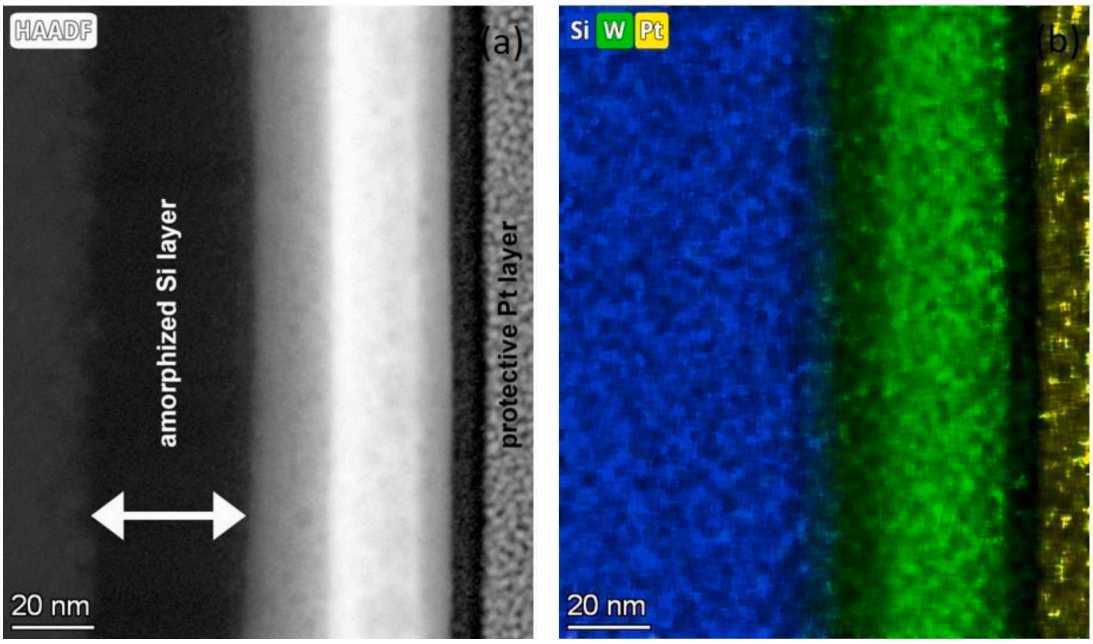

Fig. 5. a. HAADF XTEM image with the corresponding b. EDS map of the C/W 102010 sample irradiated by 120 keV 5×10^{15} Xe^{+}/cm^{2}.

specimen; 1020-Si. We can see that 5 layers are placed on a substrate. Here also the darker region corresponds to carbon while the brighter to silicon, of the higher atomic number. We can see again that the interfaces are sharp also for this layer system. The EDS map (Fig. 4b) correlates with these findings.

Fig. 5 shows a HAADF XTEM image (Fig. 5a) with the corresponding EDS map (Fig. 5b) of a 120 keV 5×10^{15} Xe^{+}/cm^{2} irradiated 102010 C/W sample. Both images show a strong change in the sample structure. At the interfaces we can see the effects of intermixing. The first carbon layer has been affected the most by the irradiation. It's thickness strongly decreased due to the ion irradiation induced material transport. We can see that the thickness of the last carbon layer was not strongly affected by the irradiation this is due to penetration depth of the ions which is for this layer structure 25 ± 10 nm calculated by SRIM. Still, the interfaces are stripes parallel to the surface, that is, the planar architecture of the sample has been preserved despite the strong material transport. We can observe that the crystalline Si substrate amorphized due to the penetrated Xe^{+} ions. The amorphization was determined based on the HRTEM image and its fast-Fourier-transform (FFT) which can be found in Fig. S1 in the Supplementary Information (SI). The HRTEM image also shows bright spots in the W layer, the bright contrast indicates a material with higher scattering cross section and/or density compared to the surrounding W. These spots can be attributed to radiation induced defects [36] like xenon bubbles.

Fig. 6 shows the XTEM image of a 120 keV 5×10^{15} Xe^{+}/cm^{2} irradiated 1020 C/Si sample with the corresponding EDS map. It can be seen again that the Si substrate is amorphized, HRTEM image and FFT see in Fig. S2 SI. At the interfaces we cannot see a change in the contrast proving slight intermixing, however, the fluence and energy were the same as for the C/W sample (Fig. 5). This suggests that the mixing effect was lower for the C/Si sample than for the C/W. However, we can see that the thickness of the carbon layer is reduced meaning that some intermixing still happened, the penetration depth of 120 keV $Xe^{+}$was 57 ± 12 nm calculated by SRIM. Concerning the radiation induced defects, we have observed xenon bubbles in the case of higher fluence irradiation (120 keV, 1×10^{16} Xe^{+}/cm^{2}). A HRTEM image for this effect is shown in

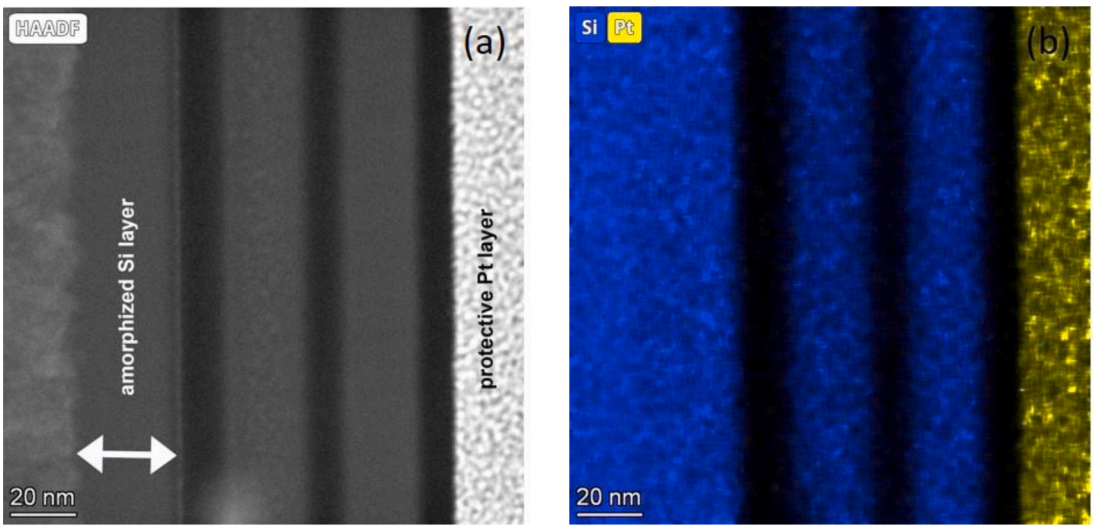

Fig. 6. HAADF XTEM image with the corresponding b. EDS map of the C/Si 1020 sample irradiated by 120 keV 5 × 10^{15} Xe^{+}/cm^{2}.

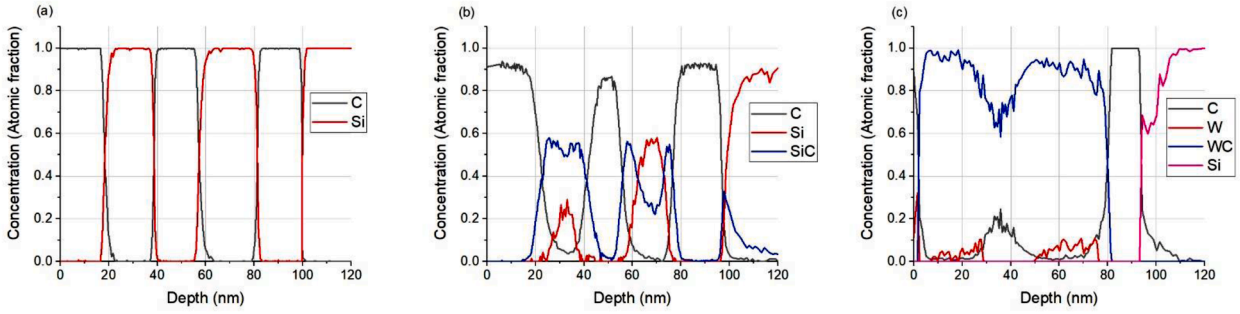

Fig. 7. AES depth profiles of the a. 2020-Si pristine b. 40 keV, 6 × 10^{16} Ar^{+}/cm^{2} 2020-Si irradiated c. 110 keV 6 × 10^{16} Ar^{+}/cm^{2} 2020-W irradiated samples.

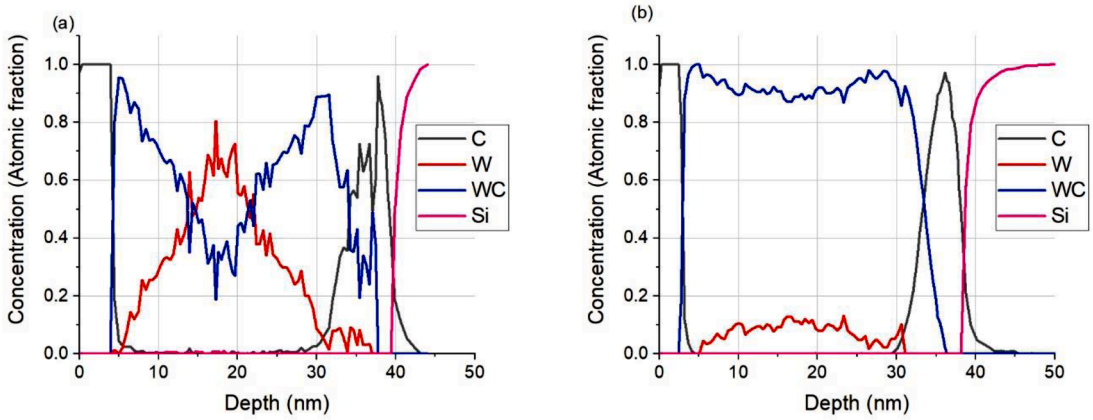

Fig. 8. AES depth profiles of the 102010-W 120 keV irradiated samples with fluencies a. 2.5 × 10^{15} Xe^{+}/cm^{2} b. 5 × 10^{15} Xe^{+}/cm^{2}.

Fig. S3 SI, here the bubbles are present like dark spots due to the low atomic number of the surrounding Si atoms [37,38].

3.2. Carbide production

For determining the component in-depth distribution before and after the irradiation AES depth profiling was performed. In the following some typical examples will be shown for the different material pairs, i.e. the C/W and C/Si, respectively.

The ion mixing and the concomitant carbide formation starts at the interfaces and growth towards the originally pure layers resulting in various distributions. The shapes of distributions strongly depend on the ion bombardment conditions and layer structure.

Fig. 7a shows the AES depth profile of a 2020-Si pristine, non-irradiated sample while a depth profile of an irradiated sample is depicted in Fig. 7b. In the pristine sample we can see that carbon and silicon layers of equal thicknesses are alternating. Fig. 7b shows the depth profile of the 2020-Si sample irradiated by 40 keV, 6 × 10^{16} Ar^{+}/cm^{2}. We can see that due to the strong material transport the thickness of Si and C layers is strongly reduced. The carbide formation at the first two

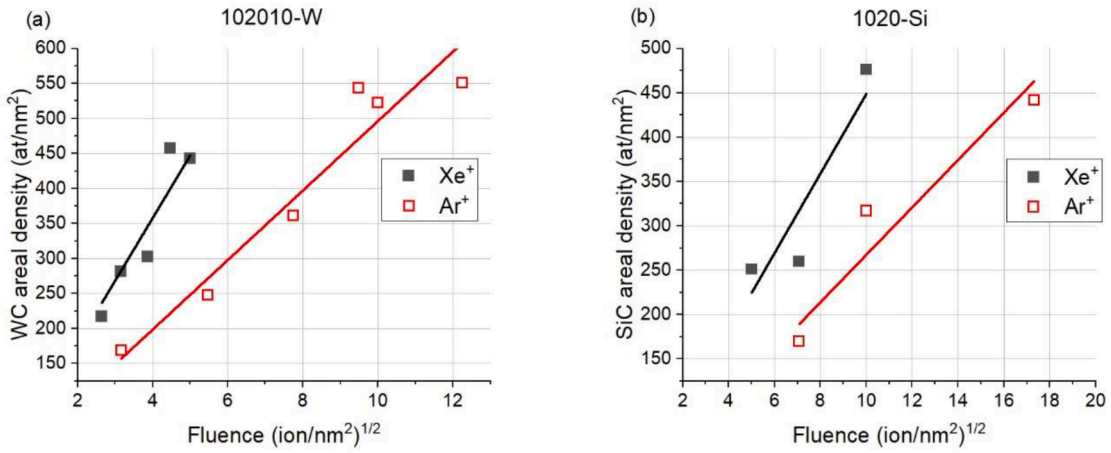

Fig. 9. a. WC areal density as a function of low fluences for sample 102010-W argon 40 keV and xenon 120 keV irradiations b. SiC areal density as a function of low fluences for sample 1020-Si argon 40 keV irradiation and xenon 120 keV irradiations.

interfaces is more pronounced than for the 3–4 interfaces. This is due to the penetration depth of 40 keV argon ions being 40 ± 13 nm [31]. As a comparison, 2020-W sample fluence (6×10^{16} Ar^+/cm^2) after irradiation as seen in Fig. 8c is the same as 2020-Si sample. For reaching all interfaces the ions energy was increased to 110 keV. We can see a complete overlap of the produced carbide layers produced at the interfaces. The first carbon layer is almost completely consumed for carbide production, almost all tungsten is used up, these findings are due to the penetration depth of 110 keV argon ions being 52 ± 25 nm [31].

The irradiation fluence has a strong influence on the carbide production. Fig. 8 shows depth profiles for sample 102010-W 120 keV 2.5×10^{15} Xe^+/cm^2 and 5×10^{15} Xe^+/cm^2 irradiations. It can be seen that the two interfaces begin to overlap after irradiation at lower fluence and at higher fluence a complete continuous carbide is formed.

The above shown results suggest that the mixing efficiency for the C/W system is very high compared to the C/Si system. The same fluence causes much more intense carbide production than for the C/Si system see Fig. 7b and c. This assumption will be further investigated. Fig. 9 shows the produced carbide amount calculated from the AES depth profiles for different ions at the first interface as a function of low fluences for the C/Si 1020 and C/W 102010 systems. Only those irradiations are plotted where the carbide produced at the different interfaces can be still well separated, eg. distributions like in Fig. 8b are not plotted. The carbide areal densities are shown as a function of the square root of fluence. The graphs clearly depict linear dependences for the different material pairs. In the case of WC areal densities (Fig. 9a) we can see that the heavy xenon ions produce more carbide than the lighter argon ion. This can be also concluded for the C/Si system (Fig. 9b). The slopes for the C/Si system are smaller than for the C/W system suggesting again the higher mixing efficiency. This will be later investigated by the SRIM simulation which provide a quantity, called deposited energy (F_d) from which the mixing efficiency can be calculated.

The linear dependences observed for both material pairs would assume that the mixing mechanism is similar. This result seems to be surprising as one would except that the big difference in the average atomic number would mean a different mixing mechanism. In the following the mixing mechanism by semi-empirical models will be examined.

3.3. Mixing mechanism – semi-empirical models

The formation of WC and SiC by low energy ion beam induced mixing of C/W and C/Si multilayers is discussed in light of various models such as ballistic mixing, thermal spike and radiation enhanced diffusion (RED). These models are well explained in literature for different systems but not employed earlier on the C/Si and C/W systems.

The contribution of radiation enhanced diffusion (RED) in mixing can be understood on the basis of critical temperature. The critical temperature is the temperature above which the defect mediated long range diffusion occurs that results in enhancement of mixing. The critical temperature T_c for the system, having cohesive energy (ΔH_{coh}) can be estimated as [4]:

$$T_C = 95.2\Delta H_{coh}[\mathrm{eV/atom}] \quad (1)$$

The calculated T_c values for the C/Si and C/W systems are 571 and 775 K, respectively. The irradiations are performed at room temperature therefore this mechanism is unlikely.

The ballistic mixing means the cascade kinetics where only binary collisions take place. Only purely ballistic aspects of atomic collisions like atomic density and mass are taken into account. The model is usually valid for materials pairs with low average atomic number $Z<20$, suggesting that for the C/Si system ($Z_{av}=10$) ballistic mixing will happen.

The ballistic mixing rate (σ^2/ϕ) can be calculated as follows:

$$(\sigma^2/\phi)_{\mathrm{ball}} = \frac{0.608 \cdot F_d \cdot \mu^{1/2} \cdot R^2}{3 \cdot \rho \cdot E_d} \quad (2)$$

where F_d is the energy deposited to recoils per ion and per unit depth at the interfaces, unit [eV/nm]; μ depends on the masses of the projectile M_1 and the target M_2, it can be calculated as $4M_1M_2/(M_1+M_2)^2$; R means the minimum separation distance for the stable Frenkel pair, its value is 1 nm; ρ is the average atomic density of the material pair [at/nm³]; E_d is the displacement energy average of the Frenkel pair formation [eV].

Thermal spike can be described as the limited volume of cascade in which all atoms are in motion. According to the fractal geometry approach of collision cascade, thermal spike begins to form neither by ion itself nor by early recoil, however, it forms by the later recoil generation. This models takes into account the thermodynamic effects like heat of mixing and cohesive energy. It is likely to occur for high Z materials, for the C/W system the Z_{av} is 40 which suggest the possibility of mixing due to thermal spike formation. Two type of thermal spike exist local and global depending differently on F_d.

Mixing rate during local thermal spike (LS) and global thermal spike (GS) formation can be calculated theoretically from the formulae given below [22]:

$$(\sigma^2/\phi)_{LS} = 0.5\left(K_1 \frac{Z^{1.77} F_d}{\rho^{2/3} \Delta H_{coh}^2}\right)\left(1 + K_2 \frac{\Delta H_{mix}}{\Delta H_{coh}}\right) \quad (3)$$

Table 2
Parameters applied in the calculation of ballistic, local and global thermal spike mixing rates for material pairs C/Si and C/W.

	ρ [at/nm^3]	E_d [eV] [28]	ΔH_{coh} [eV/atom] [29]	ΔH_{mix} [eV/atom] [30]	T_c [K] (1)
C/Si	81.3	19.0	6.0	−0.19	571
C/W	87.9	31.5	8.1	−0.62	775

Table 3
Summary of the theoretical and experimental mixing rates and mixing efficiencies for different irradiation conditions of the C/Si and C/W system.

Layer system	Ion species	Energy (keV)	F_D (keV/nm) [31,39]	Ballistic (nm^4) (2)	Local spike (nm^4) (3)	Global spike (nm^4) (4)	Experimental (nm^4)	Mixing efficiency (nm^5/keV)
102010-W	Xe^+	120	1.3	0.091	0.44	0.080	3.7	2.8
	Ar^+	40	0.59	0.032	0.20	0.016	0.80	1.4
2020-W	Ar^+	40	0.32	0.013	0.11	0.0048	0.79	2.5
	Ar^+	110	0.24	0.0098	0.082	0.0027	0.89	3.7
1020-Si	Xe^+	120	0.75	0.039	0.0099	0.0064	0.47	0.63
	Ar^+	40	0.33	0.095	0.024	0.038	0.069	0.21
2020-Si	Xe^+	120	1.0	0.13	0.030	0.059	1.0	1.0
	Ar^+	40	0.44	0.052	0.013	0.011	0.083	0.19

where Z is the average atomic number of the mixed elements, ΔH_{coh} is the cohesive energy and ΔH_{mix} is the mixing enthalpy in unit [eV/atom]. The empirical parameters K_1 and K_2 are 2.7 × 10^{-7} nm^3 keV and 50, respectively [22].

$$\left(\sigma^2/\phi\right)_{GS} = 0.5\left(K'_1\frac{F_d^2}{\rho^{5/3}\Delta H_{coh}^2}\right)\left(1+K'_2\frac{\Delta H_{mix}}{\Delta H_{coh}}\right) \quad (4)$$

where K_1'and K_2'are the empirical parameters 0.0035 nm and 27.4 respectively [22].

Table 2 summarizes the parameters applied in the equations for the different materials pairs. We can see that the average atomic densities are very similar for both material pairs. For producing a Frenkel pair in the C/W system much higher energy is needed than for the C/Si system. We can see that the cohesive energy is higher for the C/W system, than for the C/Si meaning a lower number of atomic displacement for the C/W. A big difference can be seen in the mixing enthalpy, the mixing is more favorable for high negative values suggesting that the C and W atoms mix more than the C and Si atoms. The calculated critical temperatures are also shown in the last row.

Table 3 summarizes the calculated mixing rates from the different models. The experimental mixing rate can be calculated from the measured C and Si or W AES depth profiles. We deduced the increase of the variance σ^2 of the intermixed region compared to the pristine sample as a function of the ion fluence (ϕ).

$$\Delta\sigma^2(\phi) = \sigma^2(\phi) - \sigma^2(0) \quad (5)$$

where σ^2 (ϕ) and σ^2 (0) are the variances before and after irradiation at a fluence ϕ [40].

In the case of the C/W system we can see that the experimental values of the mixing rates are close to that calculated by the local thermal spike which suggests that the local spike mechanism is dominant. In the case of C/Si mixing the ballistic mixing provides the closest value to the experimental mixing rates. The mixing efficiencies was calculated by dividing the experimental mixing rates using F_d that provides the direct comparison of the results for the same deposited energy. Now this calculation clearly proves that the mixing efficiency for argon irradiation is higher than for xenon and that the mixing is more intense for the C/W system than for the C/Si.

We have shown that the SiC and WC amount produced [24,41] due to ion mixing can be calculated from TRIDYN simulation which is based on ballistic processes. This is found despite of the fact that the mixing of the two material pair is different. This may presume that any type of carbide can be simulated regardless of the mixing process.

4. Conclusions

C/W and C/Si multilayer structures of various thicknesses have been irradiated by xenon and argon ions. Due to irradiation intermixing WC and SiC were formed at the interfaces. The thickness of the formed WC and SiC depended strongly on the irradiation conditions (energy, fluence) and layer structure. SRIM simulation was applicable to determine the proper energy of the irradiation. The thermal spike mechanism – local spike - and more efficient mixing is shown for the C/W system, while ballistic mixing for the C/Si system. A detailed recipe is provided for producing carbide-rich layers which are known as protective coatings.

CRediT authorship contribution statement

Z. Fogarassy: Investigation, Visualization, Writing – original draft, Writing – review & editing. **U. Kentsch:** Investigation. **P. Panjan:** Investigation. **A.S. Racz:** Conceptualization, Methodology, Formal analysis, Validation, Visualization, Project administration, Funding acquisition, Writing – original draft, Writing – review & editing.

Declaration of Competing Interest

The authors declare that they have no known competing financial interests or personal relationships that could have appeared to influence the work reported in this paper.

Data availability

Data will be made available on request.

Acknowledgements

The EU H2020 Project No. 824096 “RADIATE”, HZDR-Dresden and project funding of Centre for Energy Research is highly acknowledged. Authors thanks the support of VEKOP-2.3.3-15-2016-00002 of the European Structural and Investment Funds. This paper was supported by the János Bolyai Research Scholarship of the Hungarian Academy of Sciences (Z. Fogarassy). Special thanks to Dr. M. Menyhard for useful remarks, thanks are given for Dr. Z. Zolnai for discussion. Thanks are given for A. Németh for irradiating the C/Si samples. Thanks are given for L. Illés and Z. Kovács for FIB lamella preparation.

Supplementary materials

Supplementary material associated with this article can be found, in the online version, at doi:10.1016/j.surfin.2023.102773.

References

[1] K. Asokan, S.K. Srivastava, D. Kabiraj, S. Mookerjee, D.K. Avasthi, J.C. Jan, J. W. Chiou, W.F. Pong, L.C. Ting, F.Z. Chien, Study of ion beam mixing in C/Si multilayers by X-ray absorption spectroscopy, Nucl. Instrum. Methods Phys. Res. Sect. B 193 (2002) 324–328, https://doi.org/10.1016/S0168-583X(02)00799-1.

[2] M. Karlušić, R.A. Rymzhanov, J.H. O'Connell, L. Bröckers, K.T. Luketić, Z. Siketić, S. Fazinić, P. Dubček, M. Jakšić, G. Provatas, N. Medvedev, A.E. Volkov, M. Schleberger, Mechanisms of surface nanostructuring of Al2O3 and MgO by grazing incidence irradiation with swift heavy ions, Surf. Interfaces. 27 (2021), 101508, https://doi.org/10.1016/j.surfin.2021.101508.

[3] A.S. Racz, D. Zambo, G. Dobrik, I. Lukacs, Z. Zolnai, A. Nemeth, P. Panjan, A. Deak, G. Battistig, M. Menyhard, Novel method for the production of SiC micro and nanopatterns, Surf. Coat. Technol. 372 (2019) 427–433, https://doi.org/10.1016/j.surfcoat.2019.05.061.

[4] S. Gupta, D.C. Agarwal, S.A. Khan, S. Neeleshwar, S. Ojha, S. Srivastava, A. Tripathi, S. Amirthapandian, B.K. Panigrahi, D.K. Avasthi, PbTe nanocrystal formation by interface mixing of Te/Pb bilayer using low energy ions, Mater. Sci. Eng. B. 184 (2014) 58–66, https://doi.org/10.1016/j.mseb.2014.01.002.

[5] A. Arranz, C. Palacio, Ion beam mixing of Ti/Al interfaces by nitrogen irradiation, Surf. Sci. 601 (2007) 4510–4514, https://doi.org/10.1016/j.susc.2007.04.172.

[6] R.Escobar Galindo, N. Benito, D. Duday, G.G. Fuentes, N. Valle, P. Herrero, L. Vergara, V. Joco, O. Sanchez, A. Arranz, C. Palacio, In-depth multi-technique characterization of chromium–silicon mixed oxides produced by reactive ion beam mixing of the Cr/Si interface, J. Anal. At. Spectrom. 27 (2012) 390, https://doi.org/10.1039/c2ja10296j.

[7] T.T. Thabethe, T.P. Ntsoane, S. Biira, E.G. Njoroge, T.T. Hlatshwayo, V. A. Skuratov, J.B. Malherbe, Investigating the structural changes induced by SHI on W–SiC samples, Vacuum 174 (2020), 109230, https://doi.org/10.1016/j.vacuum.2020.109230.

[8] W. Han, M.J. Demkowicz, N.A. Mara, E. Fu, S. Sinha, A.D. Rollett, Y. Wang, J. S. Carpenter, I.J. Beyerlein, A. Misra, Design of radiation tolerant materials via interface engineering, Adv. Mater. 25 (2013) 6975–6979, https://doi.org/10.1002/adma.201303400.

[9] H.S. Sen, N. Daghbouj, M. Callisti, M. Vronka, M. Karlík, J. Duchoň, J. Čech, J. Lorinčík, V. Havránek, P. Bábor, T. Polcar, Interface-driven strain in heavy ion-irradiated Zr/Nb nanoscale metallic multilayers: validation of distortion modeling via local strain mapping, ACS Appl. Mater. Interfaces. 14 (2022) 12777–12796, https://doi.org/10.1021/acsami.1c22995.

[10] Y. Zhai, H. Li, Z. Tao, X. Cao, C. Yang, Z. Che, T. Xu, Design, fabrication and test of a bulk SiC MEMS accelerometer, Microelectron. Eng. 260 (2022), 111793, https://doi.org/10.1016/j.mee.2022.111793.

[11] C. Yu, X. Chen, Z. Xiao, C. Lei, C. Zhang, X. Lin, B. Shen, R. Zhang, F. Wei, Silicon carbide as a protective layer to stabilize si-based anodes by inhibiting chemical reactions, Nano Lett 19 (2019) 5124–5132, https://doi.org/10.1021/acs.nanolett.9b01492.

[12] X. Lei, S. Kane, S. Cogan, H. Lorach, L. Galambos, P. Huie, K. Mathieson, T. Kamins, J. Harris, D. Palanker, SiC protective coating for photovoltaic retinal prosthesis, J. Neural Eng. 13 (2016), 046016, https://doi.org/10.1088/1741-2560/13/4/046016.

[13] N. Daghbouj, B.S. Li, M. Callisti, H.S. Sen, M. Karlik, T. Polcar, Microstructural evolution of helium-irradiated 6H–SiC subjected to different irradiation conditions and annealing temperatures: a multiple characterization study, Acta Mater 181 (2019) 160–172, https://doi.org/10.1016/j.actamat.2019.09.027.

[14] E.C. Weigert, M.P. Humbert, Z.J. Mellinger, Q. Ren, T.P. Beebe, L. Bao, J.G. Chen, Physical vapor deposition synthesis of tungsten monocarbide (WC) thin films on different carbon substrates, J. Vac. Sci. Technol. Vac. Surf. Films. 26 (2008) 23–28, https://doi.org/10.1116/1.2806941.

[15] M.D. Abad, M.A. Muñoz-Márquez, S. El Mrabet, A. Justo, J.C. Sánchez-López, Tailored synthesis of nanostructured WC/a-C coatings by dual magnetron sputtering, Surf. Coat. Technol. 204 (2010) 3490–3500, https://doi.org/10.1016/j.surfcoat.2010.04.019.

[16] J. Nazon, M. Herbst, M.C. Marco de Lucas, S. Bourgeois, B. Domenichini, WC-based thin films obtained by reactive radio-frequency magnetron sputtering using W target and methane gas, Thin Solid Films 591 (2015) 119–125, https://doi.org/10.1016/j.tsf.2015.08.035.

[17] M. Liao, Y. Koide, J. Alvarez, Thermally stable visible-blind diamond photodiode using tungsten carbide Schottky contact, Appl. Phys. Lett. 87 (2005), 022105, https://doi.org/10.1063/1.1992660.

[18] B. Bozzini, G. Pietro De Gaudenzi, A. Fanigliulo, C. Mele, Electrochemical oxidation of WC in acidic sulphate solution, Corros. Sci. 46 (2004) 453–469, https://doi.org/10.1016/S0010-938X(03)00146-X.

[19] Y.C. Kimmel, D.V. Esposito, R.W. Birkmire, J.G. Chen, Effect of surface carbon on the hydrogen evolution reactivity of tungsten carbide (WC) and Pt-modified WC electrocatalysts, Int. J. Hydrog. Energy 37 (2012) 3019–3024, https://doi.org/10.1016/j.ijhydene.2011.11.079.

[20] Z. Lv, D. Liu, W. Tian, J. Dang, Designed synthesis of WC-based nanocomposites as low-cost, efficient and stable electrocatalysts for the hydrogen evolution reaction, CrystEngComm 22 (2020) 4580–4590, https://doi.org/10.1039/D0CE00419G.

[21] A. Arranz, C. Palacio, Nanoscale reactive ion beam mixing of Ti/Si and Si/Ti interfaces, Thin Solid Films 515 (2007) 3426–3433, https://doi.org/10.1016/j.tsf.2006.10.005.

[22] J. Conrad, W. Bolse, K.P. Lieb, T. Weber, Ion beam mixing experiments in Pt/Ni bilayers, Surf. Coat. Technol. 74–75 (1995) 941–944, https://doi.org/10.1016/0257-8972(95)08348-0.

[23] Y.-T. Cheng, X.-A. Zhao, T. Banwell, T.W. Workman, M. Nicolet, W.L. Johnson, Correlation between the cohesive energy and the onset of radiation-enhanced diffusion in ion mixing, J. Appl. Phys. 60 (1986) 2615–2617, https://doi.org/10.1063/1.337131.

[24] A.S. Racz, Z. Kerner, A. Nemeth, P. Panjan, L. Peter, A. Sulyok, G. Vertesy, Z. Zolnai, M. Menyhard, Corrosion Resistance of Nanosized Silicon Carbide-Rich Composite Coatings Produced by Noble Gas Ion Mixing, ACS Appl. Mater. Interfaces. 9 (2017) 44892–44899, https://doi.org/10.1021/acsami.7b14236.

[25] A.S. Racz, D. Dworschak, M. Valtiner, M. Menyhard, Scratching resistance of SiC-rich nano-coatings produced by noble gas ion mixing, Surf. Coat. Technol. 386 (2020), 125475, https://doi.org/10.1016/j.surfcoat.2020.125475.

[26] A.S. Racz, Z. Kerner, M. Menyhard, Corrosion resistance of tungsten carbide-rich coating layers produced by noble gas ion mixing, Appl. Surf. Sci. 605 (2022), 154662, https://doi.org/10.1016/j.apsusc.2022.154662.

[27] W. Eckstein, The Binary Collision model. Comput. Simul. Ion-Solid Interact, Springer Berlin Heidelberg, Berlin, Heidelberg, 1991, pp. 4–32, https://doi.org/10.1007/978-3-642-73513-4_2.

[28] W. Möller, W. Eckstein, Tridyn — a TRIM simulation code including dynamic composition changes, Nucl. Instrum. Methods Phys. Res. Sect. B 2 (1984) 814–818, https://doi.org/10.1016/0168-583X(84)90321-5.

[29] C. Kittel, Introduction to Solid State Physics, 8th ed, Wiley, Hoboken, NJ, 2005.

[30] A. Takeuchi, A. Inoue, Classification of bulk metallic glasses by atomic size difference, heat of mixing and period of constituent elements and its application to characterization of the main alloying element, Mater. Trans. 46 (2005) 2817–2829, https://doi.org/10.2320/matertrans.46.2817.

[31] SRIM Stopping and range of ions in matter by Ziegler, J. F. version SRIM, 2013 Software freely available www.srim.org., (n.d.).

[32] M. Menyhard, High-depth-resolution Auger depth profiling/atomic mixing, Micron 30 (1999) 255–265, https://doi.org/10.1016/S0968-4328(99)00010-4.

[33] N. Fairley, A. Carrick, N. Fairley, Recipes for XPS Data Processing, Acolyte Science, Knutsford, 2005.

[34] K.D. Childs, C.L. Hedberg, Physical Electronics, in: Incorporation (Ed.), Handbook of Auger electron Spectroscopy: A Book of Reference Data For Identification and Interpretation in Auger Electron Spectroscopy, 3. ed, Physical Electronics, Eden Prairie, 1995.

[35] L. Kotis, M. Menyhard, A. Sulyok, G. Sáfrán, A. Zalar, J. Kovač, P. Panjan, Determination of the relative sputtering yield of carbon to tantalum by means of Auger electron spectroscopy depth profiling, Surf. Interface Anal. 41 (2009) 799–803, https://doi.org/10.1002/sia.3101.

[36] N. Daghbouj, B.S. Li, M. Callisti, H.S. Sen, J. Lin, X. Ou, M. Karlik, T. Polcar, The structural evolution of light-ion implanted 6H-SiC single crystal: comparison of the effect of helium and hydrogen, Acta Mater 188 (2020) 609–622, https://doi.org/10.1016/j.actamat.2020.02.046.

[37] K. Wittmaack, H. Oppolzer, Quantitative characterization of xenon bubbles in silicon: correlation of bubble size with the damage generated during implantation, Nucl. Instrum. Methods Phys. Res. Sect. B 269 (2011) 380–385, https://doi.org/10.1016/j.nimb.2010.11.025.

[38] J. Baillet, S. Gavarini, N. Millard-Pinard, V. Garnier, C. Peaucelle, X. Jaurand, A. Duranti, C. Bernard, R. Rapegno, S. Cardinal, L.Escobar Sawa, T. De Echave, B. Lanfant, Y. Leconte, Surface damage on polycrystalline β-SiC by xenon ion irradiation at high fluence, J. Nucl. Mater. 503 (2018) 140–150, https://doi.org/10.1016/j.jnucmat.2018.01.026.

[39] W.J. Weber, Y. Zhang, Predicting damage production in monoatomic and multi-elemental targets using stopping and range of ions in matter code: challenges and recommendations, Curr. Opin. Solid State Mater. Sci. 23 (2019), 100757, https://doi.org/10.1016/j.cossms.2019.06.001.

[40] S. Dhar, M. Milosavljevic, N. Bibic, K.P. Lieb, Atomic mixing and interface reactions in Ta/Si bilayers during noble-gas ion irradiation, Phys. Rev. B. 65 (2001), 024109, https://doi.org/10.1103/PhysRevB.65.024109.

[41] A.S. Racz, Z. Fogarassy, U. Kentsch, P. Panjan, M. Menyhard, Design and production of tungsten-carbide rich coating layers, Appl. Surf. Sci. 586 (2022), 152818, https://doi.org/10.1016/j.apsusc.2022.152818.